

## Many-Body Approach to Hyperfine Structure in the $^2P$ State of Lithium\*

J. D. Lyons

IBM Research Laboratory, San Jose, California 95114

and

R. T. Pu and T. P. Das

Department of Physics, University of California, Riverside, California 92502

(Received 5 September 1968)

The Brueckner-Goldstone (BG) many-body perturbation theory has been applied in a calculation of the hyperfine structure (hfs) of lithium in the excited  $1s^22p(^2P)$  state. This is the first complete calculation of hfs by the BG theory in a nonspherical system. Our result for  $a_{1/2}$  is 45.86 Mc/sec in excellent agreement with the experimental result of  $46.17 \pm 0.35$  Mc/sec. In addition, we obtained the value  $a_{3/2} = -2.79$  Mc/sec for which no direct experimental result is currently available. The contributions from each of the magnetic hyperfine interactions and also the electric quadrupole moment interaction are presented. This approach also makes possible an analysis of the relative importance of various physical effects in each case.

### I. INTRODUCTION

The Brueckner-Goldstone (BG) linked cluster perturbation approach<sup>1</sup> for many-body problems has been applied by Kelly<sup>2</sup> to atomic calculations in beryllium and oxygen. The method was shown to yield excellent results for correlation energy, polarizability, and dipole-shielding factor. The BG theory has also been applied successfully in the past to the study of hyperfine properties of a number of atomic systems, such as the ground state ( $^2S$ ) of the lithium atom,<sup>3</sup> the excited triplet state ( $^3S$ ) of helium<sup>4</sup> and the ground states ( $^4S$ ) of nitrogen<sup>5</sup> and phosphorous atoms.<sup>6</sup> The BG method seems especially adaptable to the hfs problem both because the wave function is an eigenfunction of  $S^2$  to all orders and also because it enables a convenient separation of physical effects such as core polarization and various types of correlation. This allows an assessment of the relative importance of these effects.

In the present paper we describe the application of the BG procedure to the excited  $1s^22p(^2P)$  state of lithium.<sup>7</sup> The approach used is similar to that developed by Kelly.<sup>2</sup> This study is interesting for a number of reasons. The first reason is that, in contrast to the ground state, the  $2s$  orbital is unoccupied. Therefore, it can serve as a particle state to which the hole states may be excited. Thus a comparison of the relative importance of discrete and continuum particle states in this system with those in the ground state of lithium is expected to show significant differences. Secondly, since there is now only one state of  $s$  symmetry and one of  $p$  symmetry to consider, this makes the choice of the single-particle potential more convenient than for the ground state. In particular, we can now work entirely with hole states which are true Hartree-Fock states, and this significantly reduces the number of diagrams one has to consider. The

final and perhaps most important reason for studying the  $^2P$  state of lithium is that being nonspherical in nature it provides a vehicle for studying many-body effects on a number of other hyperfine properties<sup>8</sup>: the magnetic orbital and spin dipolar effects and nuclear electric quadrupole effects. A number of calculations of the hyperfine properties in lithium  $^2P$  are available in the literature based on one-electron theory,<sup>9-12</sup> and one configuration interaction calculation<sup>13</sup> has been given. An experimental measurement<sup>14</sup> of the hyperfine constant in the  $J = \frac{1}{2}$  state is available. The presence of several interactions makes the comparison between theory and experiment somewhat less straightforward than in the case of  $S$ -state atoms. There the theoretical result for the contact hyperfine interaction can be compared directly with the hyperfine parameter in the spin Hamiltonian. However, a level-crossing atomic-beam experiment<sup>15</sup> has been performed between the  $J = \frac{1}{2}$  and the  $J = \frac{3}{2}$  levels of lithium  $^2P$ , and this data makes possible a richer comparison between experiment and details of the theory.

Section II contains a review of the BG theory and hyperfine-structure analysis and a discussion of their application to the lithium  $^2P$  system. The relevant diagrams for the various types of hyperfine properties and their contributions are presented in Sec. III. The concluding section deals with a discussion of results and a detailed comparison with experiment.

### II. THEORY

#### A. Brueckner-Goldstone Approach to Atomic Calculations

The usual approach in calculations of atomic properties is to replace the total nonrelativistic Hamiltonian:

$$\mathcal{H} = \sum_{i=1}^N T_i + \sum_{i < j}^N \frac{1}{r_{ij}}, \quad (1)$$

$$\text{where } T_i = -\frac{1}{2} \nabla_i^2 - Z/r_i, \quad (2)$$

by a central-field-approximation Hamiltonian:

$$\mathcal{H}_0 = \sum_{i=1}^N (T_i + V_i). \quad (3)$$

Atomic units are used here and throughout. The single-particle potential,  $V_i$ , is selected in such a way that the one-electron equation,

$$(T + V) \phi_i = \epsilon_i \phi_i, \quad (4)$$

is solvable for a complete set of states  $\phi_i$  with energies  $\epsilon_i$ . A set of  $N$  of these single-particle states may then be combined to form a determinantal zero-order wave function,  $\Psi_0$ , which will satisfy the approximate Schrödinger equation:

$$\mathcal{H}_0 \Psi_0 = E_0 \Psi_0, \quad (5)$$

where the zero-order energy,  $E_0$ , is simply the sum of the corresponding  $N$  one-electron energies.

Assuming that a sufficiently judicious choice of  $V$  has been made, the difference,

$$\Delta \mathcal{H} = \mathcal{H} - \mathcal{H}_0 = \sum_{i < j}^N \frac{1}{r_{ij}} - \sum_{i=1}^N V_i, \quad (6)$$

will be a small perturbation. Then with Eq. (5) as the zero-order approximation, the solution,<sup>16</sup>  $\Psi$ , of the Schrödinger equation,

$$\mathcal{H} \Psi = E \Psi, \quad (7)$$

may be obtained through perturbation theory. In particular the BG perturbation theory gives  $\Psi$  as the linked cluster expansion,<sup>1</sup>

$$\Psi = \sum_{n=0}^{\infty} L \left( \frac{1}{\mathcal{H}_0 - E_0} \Delta \mathcal{H} \right)^n \Psi_0. \quad (8)$$

The terms of this summation are enumerated as diagrams, and the  $L$  superscript signifies that only linked diagrams are included in the sum. This diagrammatic representation of  $\Psi$  is obtained explicitly as follows. Of the set of states  $\phi_i$ , those occupied in  $\Psi_0$  are designated unexcited states; the others then being excited states. An unoccupied, unexcited state is called a hole and an occupied, excited state is a particle. A hole is represented by a downward-directed line and a particle by an upward-directed line. The basic diagram components are shown in Fig. 1. Dia-

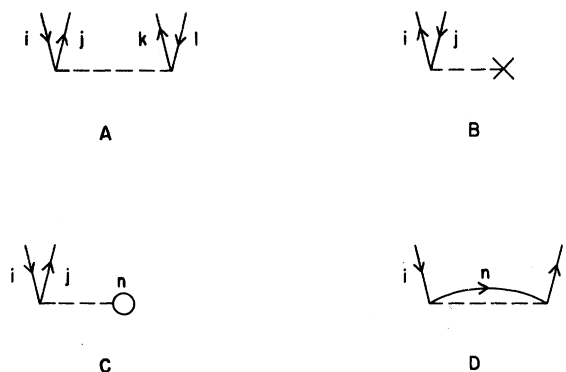


FIG. 1. Basic diagram components representing  $1/r_{12}$  interactions in A, C, and D and the  $-V$  interaction in B.

gram 1A represents a general  $1/r_{12}$  interaction connecting states  $i$  and  $j$  with states  $k$  and  $l$ . Diagram 1B represents the interaction of states  $i$  and  $j$  through the potential  $-V$ . Diagrams 1C and 1D are the direct and exchange representations of the  $1/r_{12}$  interaction of states  $i$  and  $j$  with a passive unexcited state  $n$ . The total BG wave function,  $\Psi$ , consists of all possible linked diagrams made up of these components. This description of the BG procedure is quite brief and the reader is referred to earlier literature for further details.<sup>2,3</sup>

Given the wave function, any atomic property,  $f$ , may then be obtained as the expectation value of the corresponding operator,

$$f = \langle \Psi | f | \Psi \rangle / \langle \Psi | \Psi \rangle. \quad (9)$$

Through perturbation theory the wave function is obtained as a series of successive corrections:

$$\Psi = |0\rangle + |1\rangle + |2\rangle + \dots, \quad (10)$$

where  $|k\rangle$  is used to denote the sum of all linked diagrams of order  $k$ . Thus the expectation value is given by

$$f = (\langle 0 | f | 0 \rangle + 2\langle 0 | f | 1 \rangle + \langle 1 | f | 1 \rangle + \dots) / C_N, \quad (11)$$

$$\text{with } C_N = \langle 0 | 0 \rangle + 2\langle 0 | 1 \rangle + \langle 1 | 1 \rangle + \dots. \quad (12)$$

While the wave function as defined in Eqs. (8) and (10) consists only of linked diagrams, the expectation value, Eq. (11) and, in particular, the term  $\langle 1 | f | 1 \rangle$  contains unconnected diagrams. However, the term  $\langle 1 | 1 \rangle$  in  $C_N$  in combination with  $\langle 0 | f | 0 \rangle$  provides identical unconnected diagrams of opposite sign. Thus a careful analysis of the expectation value shows that, up to second order in  $\Delta \mathcal{H}$ , Eq. (11) may be re-expressed as

$$f = \langle 0 | f | 0 \rangle + 2\langle 0 | f | 1 \rangle + \langle 1 | f | 1 \rangle + 2\langle 0 | f | 2 \rangle, \quad (13)$$

where now  $\langle 1|f|1\rangle$  contains only all possible linked diagrams. An alternative way of deriving this result is to consider  $f$  as a Hamiltonian and retain all energy diagrams involving one order in the hfs interaction.

The diagrams which contribute to the  $(m, n)$ th order of  $f$ , i. e., to  $\langle m|f|n\rangle$ , will be referred to as  $(m, n)$  diagrams. As seen from Eq. (13) the contributions to  $f$  for  $m \neq n$  are multiplied by a factor of 2 reflecting invariance with respect to time reversal. The  $(m, n)$  diagrams for all  $m$  and  $n$  are obtained from the wave function diagrams of  $|m\rangle$  and  $|n\rangle$ . All possible diagrams are drawn in which an  $|m\rangle$  diagram is connected to an  $|n\rangle$  diagram by attaching an interaction which represents the operator  $f$ .

### B. Hyperfine Interactions

The hfs arises from the various interactions which occur between the nuclear moment and the electronic spin and orbital moments. The forms of the Hamiltonian terms corresponding to these interactions may be determined through a Foldy-Wouthuysen transformation of the relativistic Hamiltonian.<sup>17</sup> Alternatively, it is possible to derive the expressions classically by utilizing the Hamiltonian for the electrons in the presence of the electromagnetic field of the nucleus. The interactions are conveniently classed in four types commonly designated: Fermi contact interaction, magnetic orbital interaction, dipole-dipole interaction, and electric quadrupole interaction. The derivations of the expressions as well as the physical meaning of each of the interactions are adequately discussed in the literature.<sup>18</sup> The Hamiltonians for the three magnetic interactions are

$$\mathcal{H}_c' = \frac{16\pi}{3} \frac{\mu_B \mu_N}{I a_B^3} \hat{\mathbf{I}} \cdot \sum_{i=1}^N \vec{s}_i \delta(\vec{r}_i), \quad (14)$$

$$\mathcal{H}_o' = 2 \frac{\mu_B \mu_N}{I a_B^3} \hat{\mathbf{I}} \cdot \sum_{i=1}^N \frac{\vec{l}_i}{r_i^3}, \quad (15)$$

$$\mathcal{H}_d' = 2 \frac{\mu_B \mu_N}{I a_B^3} \hat{\mathbf{I}} \cdot \sum_{i=1}^N \left( \frac{3(\vec{s}_i \cdot \vec{r}_i)}{r_i^5} \vec{r}_i - \frac{\vec{s}_i}{r_i^3} \right). \quad (16)$$

The electric quadrupole interaction will be discussed a little later. In Eqs. (14) - (16),  $\mu_B$  is the Bohr magneton,  $\mu_N$  is the nuclear moment,  $a_B$  is the Bohr radius,  $\hat{\mathbf{I}}$  is the nuclear spin, and  $\vec{l}_i$  and  $\vec{s}_i$  are the single-electron orbital and spin angular momentum, respectively. The subscripts  $c$ ,  $o$ , and  $d$  signify the Fermi contact, magnetic orbital, and dipole-dipole interactions in that order and will be employed in that sense throughout the paper.

The usual approach in an experimental deter-

mination of atomic hfs is to consider a spin Hamiltonian

$$\mathcal{H}' = a_J \hat{\mathbf{I}} \cdot \vec{J}, \quad (17)$$

where  $J$  is the total electronic angular momentum and  $a_J$  is called the hyperfine coupling constant. Each of the interaction Hamiltonians, Eqs. (14) - (16), may be written in the form

$$\mathcal{H}_i' = \vec{\mu}_N \cdot \vec{H}_i^{\text{eff}}, \quad (18)$$

where  $\vec{H}_i^{\text{eff}}$  is an effective magnetic field at the nucleus due to the electrons. The Wigner-Eckart theorem assures that the matrix elements of the components of  $\vec{H}_i^{\text{eff}}$  are proportional<sup>18</sup> to those of the invariant angular momentum  $\vec{J}$ . Thus we can write for the coupling constants

$$a_{iJ} = - \frac{\mu_N}{I} \frac{\langle \Psi(JM_J) | (\vec{H}_i^{\text{eff}})_z | \Psi(JM_J) \rangle}{\langle \Psi(JM_J) | J_z | \Psi(JM_J) \rangle}. \quad (19)$$

The denominator here is just  $M_J C_N$  so the coupling constants in cps for the three cases may be given explicitly as

$$a_{cJ} = (16\pi/3) \left( \mu_B \mu_N / I M_J a_B^3 \hbar \right) C_N^{-1} \times \left\langle \Psi(JM_J) \left| \sum_{i=1}^N s_{zi} \delta(r_i) \right| \Psi(JM_J) \right\rangle, \quad (20)$$

$$a_{oJ} = 2 \left( \mu_B \mu_N / I M_J a_B^3 \hbar \right) C_N^{-1} \times \left\langle \Psi(JM_J) \left| \sum_{i=1}^N \frac{l_{zi}}{r_i^3} \right| \Psi(JM_J) \right\rangle, \quad (21)$$

$$a_{dJ} = 2 \left( \mu_B \mu_N / I M_J a_B^3 \hbar \right) C_N^{-1} \times \left\langle \Psi(JM_J) \left| \sum_{i=1}^N \left( \frac{3 \vec{s}_i \cdot \vec{r}_i}{r_i^5} z_i - \frac{s_{zi}}{r_i^3} \right) \right| \Psi(JM_J) \right\rangle. \quad (22)$$

For a given  $J$  and  $M_J$  the wave function may be transformed to the  $M_L M_S$  representation resulting in a linear combination of matrix elements between the various  $M_L M_S$  states which occur for the particular  $J$  and  $M_J$ . The BG wave function for each of the  $M_L M_S$  states may then be expressed as in Eq. (10), and these matrix elements will then be given by sets of  $(m, n)$  diagrams where  $m$  and  $n$  range from zero to as high as desired. Since there are three magnetic interactions, we need three associated vertices for the corresponding matrix elements in diagrams. We have represented hfs vertices as wavy lines followed by

the appropriate letter. These are defined as follows:

$$C: \langle \phi_i | 2s_z \delta(\vec{r}) | \phi_j \rangle, \quad (23)$$

$$O: \langle \phi_i | l_z / r^3 | \phi_j \rangle, \quad (24)$$

$$D: \langle \phi_i | 2[(3\vec{s} \cdot \vec{r} / r^5)z - s_z / r^3] | \phi_j \rangle. \quad (25)$$

It is also of interest to consider here the consequence of applying, in addition, an external magnetic field. If the field is sufficiently strong that the Zeeman terms are large compared with the spin-orbit interaction, then the former may no longer be treated as a small perturbation. However, the Zeeman terms do not commute with  $J^2$  and therefore  $J$  is no longer a good quantum number of the wave function. This is exactly the situation which occurs in connection with level crossing experiments<sup>15</sup> in Li  $^2P$  state. In this case the quantities which are of direct interest are these same matrix elements between the various possible  $M_L M_S$  states including any non-diagonal ones which may occur. Thus the quantities which are directly obtained in this BG calculation are explicitly applicable in an analysis of such a level-crossing measurement.

It remains to consider the last of the hyperfine interactions, that due to the nuclear electric quadrupole moment  $Q$ . The corresponding term in the spin Hamiltonian has the form<sup>18</sup>

$$\mathcal{H}_Q = [e^2 q Q / 4I(2I - 1)] (3I_z^2 - \vec{I} \cdot \vec{I}), \quad (26)$$

where  $q$  is the field gradient at the nuclear site due to the electron. If an accurate value for  $q$  is known, then the quadrupole moment may be determined through a measurement of  $e^2 q Q$ . Thus the quantity of theoretical interest is the electronic field gradient at the nucleus. The corresponding expectation value<sup>18</sup> is

$$q = \frac{\left\langle \Psi \left| \sum_{i=1}^N 2 \left( \frac{4\pi}{5} \right)^{1/2} \frac{Y_{20}(\Omega_i)}{r_i^3} \right| \Psi \right\rangle}{\langle \Psi | \Psi \rangle}. \quad (27)$$

In the literature one often deals with the shielding factor,<sup>19</sup>

$$\gamma = (q - q_0) / q_0 \quad (28)$$

where

$$q_0 = \frac{\left\langle \Psi_0 \left| \sum_{i=1}^N 2 \left( \frac{4\pi}{5} \right)^{1/2} \frac{Y_{20}(\Omega_i)}{r_i^3} \right| \Psi_0 \right\rangle}{\langle \Psi_0 | \Psi_0 \rangle}. \quad (29)$$

In the corresponding diagrams the single-particle matrix elements of the gradient operator are given by an hfs vertex designated by  $Q$  and signifying

$$Q: \langle \phi_i | 2(4\pi/5)^{1/2} Y_{20}(\Omega) / r^3 | \phi_j \rangle. \quad (30)$$

### C. Single-Particle Potential and Wave Function

The electronic configuration of the lithium atom in the  $^2P$  state is  $1s^2 2p$ . These electrons can couple to give  $J = \frac{3}{2}$  or  $\frac{1}{2}$ . Since the state of maximum  $M_J$  involves a combination of a minimum number of  $M_L M_S$  states, we prefer to consider the cases  $J = \frac{3}{2}$ ,  $M_J = \frac{3}{2}$  and  $J = \frac{1}{2}$ ,  $M_J = \frac{1}{2}$ . The zero-order wave functions for these states may be represented as

$$\Psi_0(J = \frac{3}{2}, M_J = \frac{3}{2}) = \Psi_0(M_L = 1, M_S = \frac{1}{2}) \quad (31)$$

and

$$\begin{aligned} \Psi_0(J = \frac{1}{2}, M_J = \frac{1}{2}) &= \sqrt{\frac{2}{3}} \Psi_0(M_L = 1, M_S = -\frac{1}{2}) \\ &\quad - \sqrt{\frac{1}{3}} \Psi_0(M_L = 0, M_S = \frac{1}{2}). \end{aligned} \quad (32)$$

The three  $M_L M_S$  states which occur on the right in Eqs. (31) and (32) are determinantal functions, composed of one-electron functions,  $\phi_i$ , for the paired  $1s$  core and the valence states  $2p_1^+$ ,  $2p_1^-$ , and  $2p_0^+$ , respectively.

Starting with each of these three restricted Hartree-Fock (RHF) determinantal functions a perturbation hierarchy of correction terms may be generated through Eq. (8). Each of these wave-function correction terms is expressed as a sum of diagrams of the appropriate order; and the particular diagrams which contribute are dependent upon the choice of the single-particle potential. It is only necessary to carry out this entire procedure for one of the  $M_L M_S$  states since all physical information is contained in the reduced matrix elements which depend only on  $L$  and  $S$ . This is, of course, a consequence of the Wigner-Eckart theorem. This point will be discussed in terms of diagrams subsequently. First the calculation of the wave-function diagrams of first and second order will be discussed in terms of the special case of the determinant ( $M_L = 1$ ,  $M_S = \frac{1}{2}$ ).

The one area in which the BG procedure allows considerable freedom of choice is in the selection of a single-particle potential. Of course, whatever is included in or excluded from  $V$  is immediately compensated by  $\Delta\mathcal{H}$  as shown in Eq. (6). Thus several important considerations emerge relative to the choice of  $V$ . This topic has been considered in detail elsewhere.<sup>2,3</sup> Suffice it to say at this point that two factors were of major concern in selection of the single-particle potential for Li ( $^2P$ ). First it was desired to achieve maximum cancellation between single-excitation

wave-function diagrams; which is equivalent to requiring maximum agreement with the Hartree-Fock potential. Secondly, it was desired to achieve the maximum rate of convergence possible in the perturbation theory, and this corresponds to requiring the greatest possible similarity to real physical single-particle states.

The choice of potential which seems best to meet both of these requirements is one in which all  $s$  states are generated in the presence of Coulomb interactions with one  $1s$  electron and one spherically averaged  $2p$  electron and half an exchange interaction with the spherically averaged  $2p$  electron. Correspondingly, all states of nonzero angular momentum experience Coulomb interactions with the  $1s$  core and an exchange interaction with one of the  $1s$  electrons. A complete orthogonal set of states is still obtained even though the radial part of the potential differs for  $s$  and non- $s$  states since between these states orthogonality is assured through the angular dependence.

The potential just described may be written explicitly in terms of matrix elements as

$$\begin{aligned} \langle j_s | V_s | i_s \rangle = & \langle j_s(1)1s(2) | r_{12}^{-1} | i_s(1)1s(2) \rangle \\ & + \langle j_s(1)2p(2) | r_{12}^{-1} | i_s(1)2p(2) \rangle \\ & - \frac{1}{2} \langle 2p(1)j_s(2) | r_{12}^{-1} | i_s(1)2p(2) \rangle, \end{aligned} \quad (33)$$

and  $\langle j_l | V_s | i_l \rangle$

$$\begin{aligned} = & 2 \langle j_l(1)1s(2) | r_{12}^{-1} | i_l(1)1s(2) \rangle \\ & - \langle 1s(1)j_l(2) | r_{12}^{-1} | i_l(1)1s(2) \rangle. \end{aligned} \quad (34)$$

Figures 2(A) and 2(B) are diagrammatic representations of Eqs. (33) and (34), respectively. Whenever a  $V$  interaction occurs in a diagram it is replaced by the corresponding set of diagrams shown in Fig. 2. Thus many diagrams containing direct and exchange interactions with passive states are cancelled explicitly by the potential  $V$ . This greatly reduces the number of diagrams to be evaluated numerically.

It should be noted that the potential defined by Eqs. (33) and (34) or equivalently by Figs. 2(A) and 2(B) is exactly the restricted Hartree-Fock potential when Eq. (4) is solved for the  $1s$  or  $2p$  states. However, excited states are also obtained in a potential which includes interactions with only two other electrons. This is physically reasonable and provides asymptotically a Coulomb potential corresponding to a unit positive ionic charge. One consequence of this is that the set of states consists of both bound and continuum states. Another is that certain ladder diagrams which often occur as corrections to the potential<sup>2, 3</sup> are not present

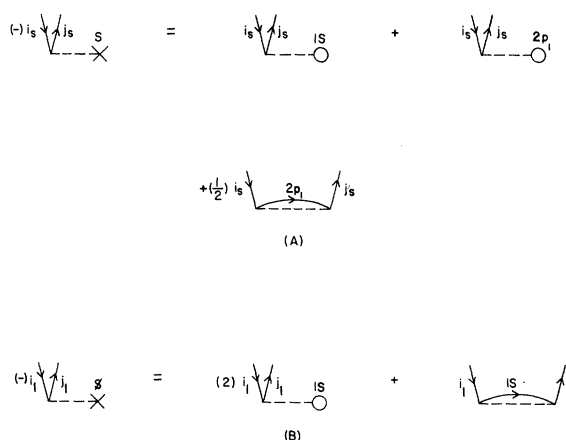


FIG. 2. Diagrammatic representation of the single-particle potential for  $s$  and non- $s$  states.

in this case.

Obtaining the first-order wave function is now simply reduced to a systematic procedure of drawing all possible diagrams which begin with the reference state (taken as the vacuum state) and contain a single interaction of the types listed in Fig. 1. When the three  $V$  diagrams which occur are expanded in terms of direct and exchange interactions with passive states and all possible cancellations made, the total first-order wave function is given as the set of diagrams exhibited in Fig. 3. A few comments about these diagrams are pertinent. Diagram 3A represents the well-known exchange polarization of the  $1s$  core by the  $2p$  electron and is a consequence of using an RHF potential, Eq. (33), which does not

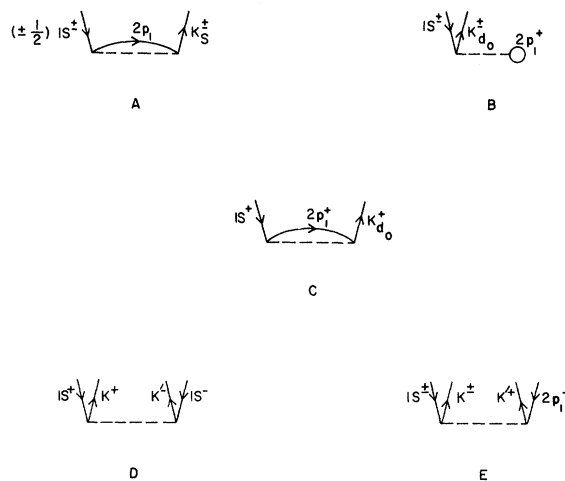


FIG. 3. Complete set of first-order wave-function diagrams after cancellation made possible by the choice of single-particle potential.

discriminate between states of different spin. Figure 3B results from the use of a central approximation for  $V$  and represents an electrostatic polarization of the  $1s$  core. Both of these effects act in combination in diagram 3C which can be described as anisotropic exchange polarization. The last two diagrams represent many-body effects which are always present independent of the choice of  $V$ .

Obtaining the second-order wave function requires a procedure entirely analogous to that just described. All possible diagrams are drawn beginning with each of the diagrams of Fig. 3 and with one more interaction added. The final complete set of second-order wave-function diagrams is obtained after making all the cancellations arising from  $V$  diagrams. Since there are 78 diagrams which could contribute to a one-electron property such as hfs, only a few diagrams, representative of certain classes of physical effects, are shown in Fig. 4. The first diagram is an example of the hybrid effect of exchange polarization and consistency between the  $1s$  orbitals. Figure 4B is a similar combination of exchange polarization with intrashell correlation. The other four diagrams shown indicate various types of direct and exchange correlation effects.

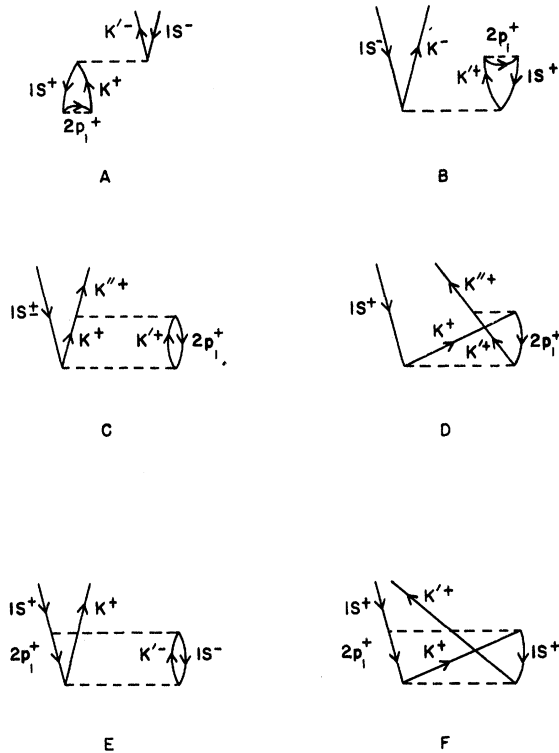


FIG. 4. Representative second-order wave-function diagrams.

#### D. Relationship Between hfs in $J = \frac{3}{2}$ and $J = \frac{1}{2}$ Levels

It would appear from Eqs. (20)–(22) for  $a_J$  that we would have to carry out a BG calculation for the  $J = \frac{3}{2}$  level and another for  $J = \frac{1}{2}$  starting from Eq. (31) and (32), respectively, for  $\Psi_0$ . This would further entail calculating off-diagonal matrix elements between two different  $M_L M_S$  states for the case of  $J = \frac{1}{2}$  which can certainly be done. However, a proper application of the Wigner-Eckart theorem entirely obviates the need for a BG calculation for  $J = \frac{1}{2}$ .

To demonstrate this it is convenient to start with Eq. (18) for the hfs Hamiltonian  $\mathcal{H}'$ . The matrix elements of  $\mathcal{H}'$  that are of interest in Eqs. (20)–(22) for  $a_J$  are actually matrix elements of  $\vec{H}^{\text{eff}}$  over the electronic wave function, since the nuclear moment is handled classically. Inasmuch as  $\vec{J}$  represents the invariant angular momentum of the system, the Wigner-Eckart theorem yields

$$\langle JM_J | \vec{H}_i^{\text{eff}} | JM_J' \rangle = F_i(J) \langle JM_J | \vec{J} | JM_J' \rangle, \quad (35)$$

where  $F_i(J)$  depends differently on  $J$  for each of the three types of magnetic interactions, since they depend on electron spin and space coordinates in different tensorial forms.

In addition, the actual value of  $F_i(J)$  for each interaction will differ from one-electron to many-electron theory, However, the dependence on  $J$  is the same in either case. This means that the ratios  $F_i \frac{1}{2} / F_i \frac{3}{2}$ , and, hence,  $a_i \frac{1}{2} / a_i \frac{3}{2}$ , are constants and can be simply evaluated using the one-electron theory. Thus substituting Eqs. (31) and (32) for  $\Psi_0$  in Eqs. (20)–(22) we obtain for the ratios

$$R_c = a_{c \frac{1}{2}} / a_{c \frac{3}{2}} = -1, \quad (36)$$

$$R_o = a_{o \frac{1}{2}} / a_{o \frac{3}{2}} = 2, \quad (37)$$

$$R_d = a_{d \frac{1}{2}} / a_{d \frac{3}{2}} = -10. \quad (38)$$

Therefore, the values of  $a_i \frac{1}{2}$  are given directly from those for  $a_i \frac{3}{2}$ .

In utilizing the results of one-electron theory to decide on the ratios of hyperfine constants of different  $J$  levels, a note of caution should be sounded. For instance, in the one-electron theory, because both orbital and dipolar hyperfine terms involve  $\langle 2p | 1/r^3 | 2p \rangle$ , it follows that  $a_{o \frac{3}{2}} = -5a_{d \frac{3}{2}}$ . On combining this with Eqs. (37) and (38), it is found that  $a_{(o+d) \frac{3}{2}} = 5a_{(o+d) \frac{1}{2}}$ . These relations, however, should not be expected to hold except in one-electron theory since they relate operators of different tensorial character. Thus the use of these relations in analyzing experimental data<sup>15</sup> can introduce some error. This point was emphasized in an empirical manner by

Harvey<sup>20</sup> who suggested using two different quantities  $\langle 2p | 1r_o^{-3} | 2p \rangle$  and  $\langle 2p | 1/r_d^3 | 2p \rangle$  for the orbital and dipolar terms  $a_o$  and  $a_d$  in the one-electron expressions.

While we do not need to evaluate  $a_{1/2}$  explicitly because of the Wigner-Eckart theorem, one does need matrix elements over  $M_L M_S$  states for the interpretation of level-crossing experiments. There the invariance of  $J$  is broken by the introduction of Zeeman terms associated with a strong magnetic field. Denoting  $\Psi_0(M_L=1, M_S=\frac{1}{2})$ ,  $\Psi_0(M_L=1, M_S=-\frac{1}{2})$ , and  $\Psi_0(M_L=0, M_S=\frac{1}{2})$  by  $D_1$ ,  $D_2$ , and  $D_3$ , respectively, we require essentially the matrix elements  $\langle D_1 | \mathcal{H}' | D_1 \rangle$ ,  $\langle D_2 | \mathcal{H}' | D_2 \rangle$ ,  $\langle D_3 | \mathcal{H}' | D_3 \rangle$ , and  $\langle D_2 | \mathcal{H}' | D_3 \rangle$  for each of the three operators. Since  $L^2$  and  $S^2$  still provide good quantum numbers, one can now use the Wigner-Eckart theorem in terms of the  $L, S, M_L, M_S$  representation to relate  $\langle D_m | \mathcal{H}' | D_n \rangle$  ( $m, n \neq 1$ ) to  $\langle D_1 | \mathcal{H}' | D_1 \rangle$ . Utilizing the same information required in the derivation of Eqs. (36)–(38), we have found

$$\begin{aligned} (\mathcal{H}'_c)_{22} &= -3(\mathcal{H}'_c)_{11}, & (\mathcal{H}'_c)_{33} &= +3(\mathcal{H}'_c)_{11}, \\ (\mathcal{H}'_c)_{23} &= 0, & (\mathcal{H}'_o)_{22} &= 3(\mathcal{H}'_o)_{11}, \\ (\mathcal{H}'_o)_{33} &= (\mathcal{H}'_o)_{23} = 0, & (\mathcal{H}'_d)_{22} &= -3(\mathcal{H}'_d)_{11}, \\ (\mathcal{H}'_d)_{33} &= -6(\mathcal{H}'_d)_{11}, & (\mathcal{H}'_d)_{23} &= \frac{3}{2}\sqrt{2}(\mathcal{H}'_d)_{11}. \end{aligned} \quad (39)$$

Even though this discussion has shown that calculation of diagrams for the  $J=\frac{1}{2}$  state is unnecessary, it is interesting to consider them for two reasons. First, this is a convenient example in which to investigate the effect of a multideterminantal zero-order state. Secondly, it serves as a check on the correctness of our perturbation-theory calculation. It is certainly possible to apply the BG technique to a multideterminant state. In terms of hfs calculations for the contact and orbital operators where mixing of configurations is not possible, it is simply a matter of summing sets of diagrams for each zero-order determinant. The dipolar operator is a little more involved in that matrix elements between different  $M_L M_S$

states occur. Our convention for representing the resulting off-diagonal diagrams is to consider  $D_2$  as the vacuum state. Thus diagrams which connect  $D_2$  with  $D_3$  appear as excitations from  $D_2$  to  $D_3$  and will therefore have two open lines at the bottom: an upward-directed line representing the  $2p_1^-$  state and a downward-directed line representing the  $2p_0^+$  state.

Demonstrating agreement with the Wigner-Eckart theorem in the case of the contact and orbital operators is quite simple and is exemplified by the special cases shown as Figs. 5A and 5B. The dipolar case is also straightforward in terms of the convention described above for off-diagonal diagrams and an example is given as Fig. 5C.

Figures 5A–5C are diagrammatic forms of Eqs. (36)–(38), respectively. This may be shown in each case by evaluating the diagrams. For example, in the contact case, Fig. 5A, all diagrams are expressible as a product of constants arising from the contact operator and the angular integration multiplying a common factor

$$\phi_{1s}(0)\phi_{ks}(0)(1s2p | 2pks)^1 / (\epsilon_{1s} - \epsilon_{ks}).$$

Dropping this and the constant  $(16\pi/3)\mu_B\mu_N/Ia_B^3C_N$  from each side of the equation, there remains

$$\begin{aligned} M_J^{-1} [(-\frac{1}{3})(\frac{1}{6}) + (\frac{1}{3})(-\frac{1}{6}) + (\frac{1}{6})(\frac{1}{6}) - (\frac{1}{6})(-\frac{1}{6})]_{M_J=\frac{1}{2}} \\ = (-1)M_J^{-1} [(\frac{1}{2})(\frac{1}{6}) - (\frac{1}{2})(-\frac{1}{6})]_{M_J=\frac{3}{2}}, \end{aligned} \quad (40)$$

which is, of course, an identity. A similar treatment verifies Figs. 5B and 5C.

Finally we consider the relationship of the field gradient in the two  $J$  levels. The Wigner-Eckart theorem applied in the same manner as for the magnetic hyperfine operators starting with Eq. (27) gives

$$q_{1/2} = 0. \quad (41)$$

This vanishing of  $q_{1/2}$  can be seen in the one-electron theory by observing that  $\Psi_0(J=\frac{1}{2}, M_J=\frac{1}{2})$  of Eq. (32) has a spherical charge distribution, which means that

$$\langle \Psi_0(J=\frac{1}{2}, M_J=\frac{1}{2}) | L^2 | \Psi_0(J=\frac{1}{2}, M_J=\frac{1}{2}) \rangle = 0. \quad (42)$$

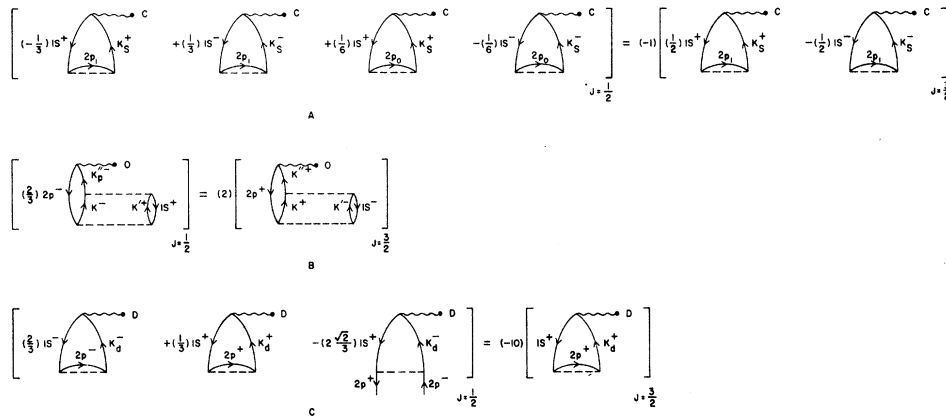


Fig. 5. Relationship between diagrams for  $J=\frac{1}{2}$  and those for  $J=\frac{3}{2}$  for contact, orbital, and dipole-dipole operators.

Since  $L^2$  commutes with  $\mathcal{H}$  and  $\mathcal{H}_0$  and hence with  $\Delta\mathcal{H}$ , no nonspherical perturbation can be introduced by  $\Delta\mathcal{H}$  through Eq. (8). Thus  $q_{1/2}$  is still zero after incorporating many-body effects.

### III. DESCRIPTION AND EVALUATION OF DIAGRAMS

Using the BG wave function up to second order, expectation values of the four hyperfine interaction operators have been calculated. In the convention described previously, all diagrams of order (0, 0), (0, 1), (1, 1), and (0, 2) have been evaluated. Some diagrams of higher order have been evaluated as a check on convergence of the results. The numerical procedures employed have been discussed in previous papers.<sup>3,4</sup> Briefly, the Hartree-Fock integro-differential equation for the single-particle states was solved numerically for both bound and continuum states. The momentum values for the continuum states were selected such that a twelve-point Gauss-Laguerre integration technique could be employed in  $k$  space. This section contains four subsections, each dealing with one of the hfs interactions. In each case the diagrams and their values are given together with a discussion of their meaning.

#### A. Fermi Contact Interaction

There are no contributing (0, 0) diagrams for the Fermi contact interaction since the sum of these corresponds to the net spin density of the RHF function at the nucleus. This is, of course, zero for Li  $1s^2 2p(^2P)$ . Thus the lowest-order, and most significant, contribution to the contact term is the (0, 1) diagram given as C1 in Fig. 6. In this and all similar figures, the diagrams are shown along with their net contribution to the hyperfine coupling constant in Mc/sec. These values include contributions due to time reversal whenever applicable. Diagram C1 represents core polarization and its contribution is over 90% of the total contact term. The source of this diagram may be seen from Fig. 3A of the first-order wave function. Contributions from the two spin states add due to the spin dependence of the contact operator.

It is possible to sum certain classes of diagrams, called ladder diagrams, to all orders by techniques described in the literature.<sup>2,3</sup> Because of our choice of potential, ladders of the core-polarization diagram in the present case can only occur in odd orders. This total effect is negligible since the combination of hole-hole and diagonal-hole particle ladders changes the diagram value by less than 0.002 Mc/sec.

The (1, 1) contact diagrams are given as C2 through C6 of Fig. 6. Diagram C2 is an interplay between core polarization and intra-shell correlation and will be referred to as a hybrid dia-

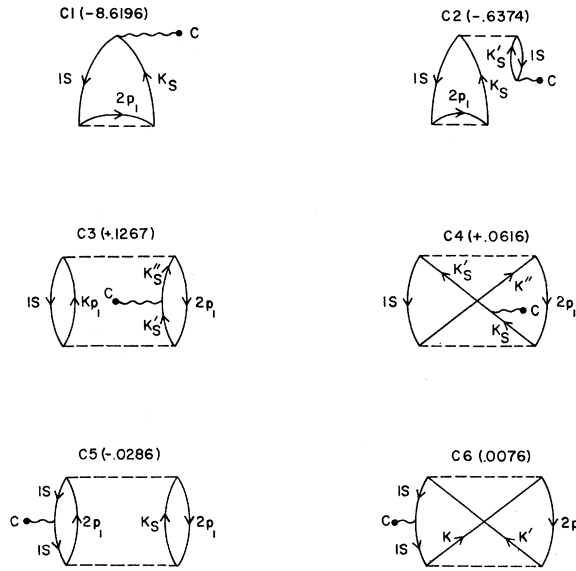


FIG. 6. (0, 1) and (1, 1) diagrams for the Fermi contact interaction and their values in Mc/sec.

gram. Diagrams C3 and C4 are pure direct and exchange intershell correlation contributions, respectively. The last two diagrams are similar to these except with the contact interaction attached to the 1s hole line. Diagram C2 is seen to supply a fairly large amount. This may be understood as follows. One of the 1s electrons is exchange polarized by the unpaired 2p electron thus acquiring modified s character. This modified 1s electron then transmits its exchange polarization to the other 1s electron through their large mutual correlation leading to additional spin density at the nucleus. In general we have found that whenever a diagram includes the exchange polarization element, Fig. 3A, its contribution is substantial relative to diagrams of the same order.

Diagrams C7 through C14 listed in Fig. 7 comprise the (0, 2) contribution to the contact interaction. Diagrams C7 and C8 are hybrid effects of core polarization with consistency in the former and correlation in the latter. Diagrams C9 and C10 represent intra- and intershell correlation, respectively, with C11 being the exchange counterpart of C10. Diagram C12 is an exclusion principle violating<sup>2,3</sup> (EPV) exchange correlation diagram. Finally diagrams C13 and C14 are direct and exchange hole-hole correlation contributions. Diagrams C11 and C12 are shown as individually substantial though mutually cancelling in effect. Their opposite signs arise from the additional internal hole line in C12. That they are of similar magnitude can be understood from the fact that, when  $k$  is a  $p$  state and  $k'$  is an  $s$  state in C11, all interactions are the same except for the middle vertex. In this vertex the integration over  $k_s k_s''$

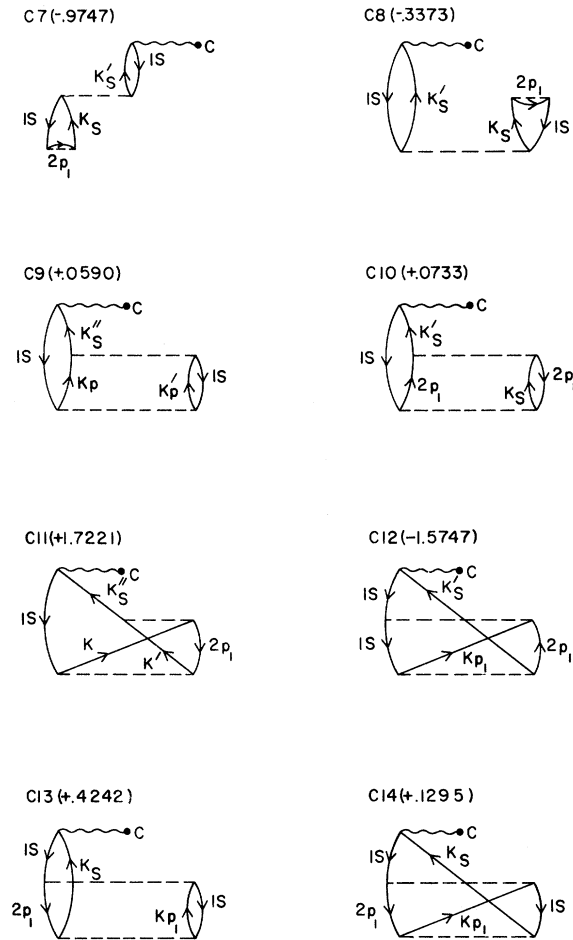


FIG. 7. (0, 2) diagrams for the Fermi-contact interaction and their values in Mc/sec.

gives a contribution comparable with that from  $1s\ 1s$ . It was found that this particular contribution to C11 is the predominant one and cancels much of C12.

Considering the cancellation of C11 and C12, the largest contribution from (0, 2) diagrams again comes from the hybrid diagrams as was the case in (1, 1) order. Altogether hybrid diagrams, C2, C7, and C8, amount to about  $-1.95$  Mc/sec, so this is certainly a significant effect. Actually it may be demonstrated that diagrams C2, C7, and C8 are not all independent. All three diagrams involve products of the same three matrix elements and their energy denominators are simply related. The energy denominator of C2 is

$$[(2\epsilon_{1s} - \epsilon_{k_s} - \epsilon_{k_s'}) (\epsilon_{1s} - \epsilon_{k_s})]^{-1},$$

and that of C8 is

$$[(\epsilon_{1s} - \epsilon_{k_s'}) (2\epsilon_s - \epsilon_{k_s} - \epsilon_{k_s'})]^{-1}.$$

Adding these together gives

$$(2\epsilon_{1s} - \epsilon_{k_s} - \epsilon_{k_s'})^{-1} [(\epsilon_{1s} - \epsilon_{k_s})^{-1} + (\epsilon_{1s} - \epsilon_{k_s'})^{-1}],$$

which reduces to

$$[(\epsilon_{1s} - \epsilon_{k_s})(\epsilon_{1s} - \epsilon_{k_s'})]^{-1};$$

and this is exactly the energy denominator of C7. Thus C7 is identically the sum of C2 and C8. This is shown diagrammatically in Fig. 8. The fact that the numerical values given with Fig. 8 satisfy this relation serves as a verification of our numerical accuracy.

Another consequence of a particular choice for the single-particle potential is the specific composition of the phase space over which diagrams are to be integrated. In the present case the only unexcited states are  $1s^+$ ,  $1s^-$ , and  $2p_1^+$ . Therefore all other  $2p$  electrons must be considered as excited states. In general a tremendous amount of cancellation of diagrams occurs in summations over  $m_s$  and  $m_l$ . In fact frequently the only contribution remaining from a given diagram is a result of this "asymmetry of phase space" just described. We refer to such specific diagrams remaining after cancellation of a general sum over allowed phase space for a diagram as "residue diagrams." Diagram C9 of Fig. 7 is a good example of this concept. Actually there are two possible diagrams of this type, corresponding to having the contact interaction line attached to a positive- or negative-spin  $1s$  electron. In general the contributions from these two diagrams would cancel for each possible set of particle states  $k_p$ ,  $k_p'$ , and  $k_s''$ . However the  $1s^-$  electron can be excited to a  $2p_1^-$  state while this excitation is not available to a  $1s^+$  electron. Thus C9 actually reduces to the difference between two residue diagrams; one corresponding to replacing  $k_p$  with  $2p$  and the other with  $2p$  substituted for  $k_p'$ . The contributions of these two diagrams are  $+0.1491$  and  $-0.0901$  Mc/sec, respectively, combining to give the value shown in Fig. 7. Thus the small but finite contribution from diagram C9 owes its origin entirely to the asymmetry of our phase space.

In general a diagram must be summed over states of all angular momentum as well as all  $k$  values. In most cases selection rules eliminate all but one or two possible values of  $l$  in a diagram. However, a few diagrams remain in which contribu-

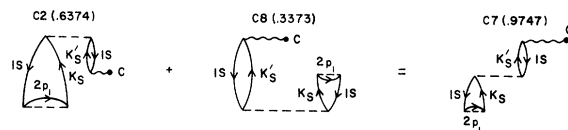


FIG. 8. Relationship of hybrid (1, 1) and (0, 2) contact diagrams.

tions from any  $l$  value are allowed. Diagram C11 is the only example of this situation in the contact case. In this work  $s$ ,  $p$ ,  $d$ , and  $f$  states were included. To demonstrate the effect of the cutoff at  $l=3$  a comparison of contributions to diagram C11 from various angular momentum states is given in Table I. It is seen that contributions for increasing  $l$  values decrease substantially, leading us to expect that inclusion of higher angular momentum states would have a minor effect on the total value of this diagram.

In view of the substantial size of some of the (1, 1) and (0, 2) diagrams, we felt it desirable to examine some higher-order diagrams of similar types. We evaluated certain (0, 3) and (1, 2) diagrams which are built out of the interactions found in the larger (1, 1) and (0, 2) diagrams; specifically diagrams C2, C7, C8, and C12. These diagrams and their values are given as Fig. 9. It is seen that none of them are very significant. Thus assuming large amounts of cancellation in these orders as found in (1, 1) and (0, 2), we expect the total contribution to be of the order of 1%.

**B. Magnetic Orbital Interaction**

The magnetic orbital interaction diagrams in contrast to the contact diagram do not benefit from any cancellation of positive-spin and negative-spin contributions since the operator is spin-independent. Another complete reversal in the nature of the contributions occurs between contact and orbital interactions in that only  $s$  electrons may contribute in the former, while due to the  $l_z$  operator in the orbital case there is no contribution from  $s$  electrons at all.

In (0, 0) order the  $1s$  electrons cannot contribute due to the form of the operator, so the only (0, 0) diagram is the direct  $2p_1$  contribution given as diagram O1 in Fig. 10. This diagram corresponds to the total orbital hfs contribution in the RHF method. There is no contribution possible in (0, 1) order.

Diagrams O2 to O9 of Fig. 10 comprise the (1, 1) contribution to the orbital interaction. Diagram O2 is the hybrid effect of electrostatic polarization of the  $1s$  core contributing through its intershell correlation with the  $2p_1$  electron. The corresponding exchange effect is given as diagram O3. Diagram O4 is intrashell correlation and the only contribution here is from residues. Dia-

TABLE I: Contributions to diagram C11 (see Fig. 7) from all allowed angular momentum states up to  $f$ .

$l_k$	$l_k'$	Contribution (Mc/sec)
$s$	$p$	-0.2229
$p$	$s$	+1.2363
$p$	$d$	+0.3024
$d$	$p$	+0.2716
$d$	$f$	+0.0690
$f$	$d$	+0.0656

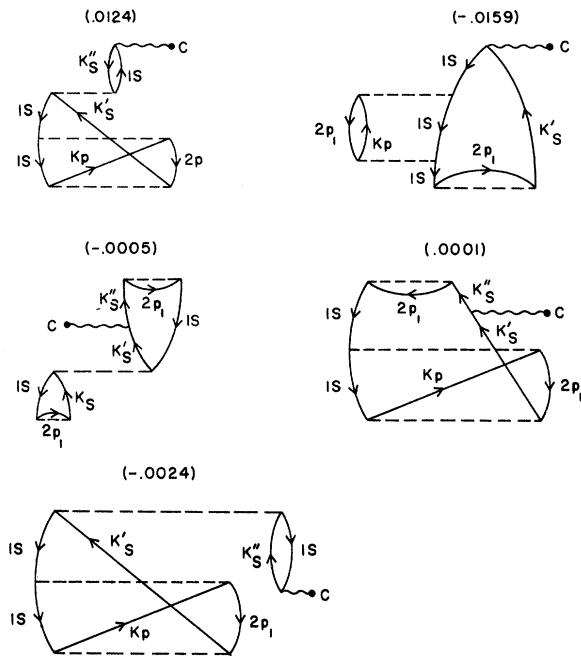


FIG. 9. Representative major higher-order diagrams.

grams O5 - O9 represent direct and exchange intershell correlation contributing through either the  $1s$  or  $2p_1$  electrons. The dominant contribution in this order is from that part of diagrams O6 and O7 which represents purely radial excitations of the  $2p$  orbital.

The (0, 2) orbital diagrams are given in Fig. 11. Diagrams O10 and O11 are direct and exchange hybrid diagrams of a type similar to diagram C8. The rest of the (0, 2) diagrams, O12 through O15, correspond to various pure correlation effects. The largest contribution again comes from the intershell correlation diagram O15 in which the  $2p_1$  electron undergoes purely radial correlation.

**C. Dipole - Dipole Interaction**

The diagrams of the dipole-dipole interaction

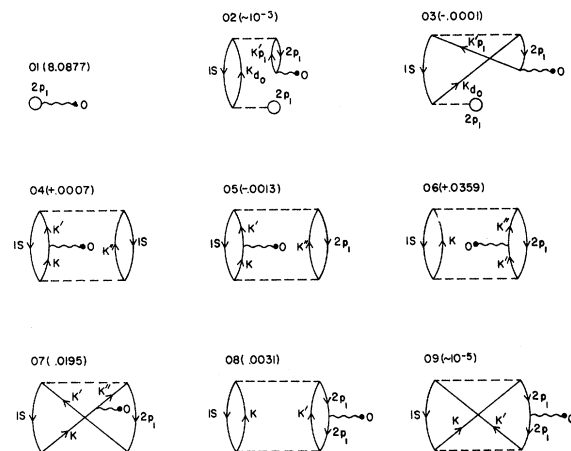


FIG. 10. (0, 0) and (1, 1) diagrams for the magnetic orbital interaction.

have features in common with both of the operators discussed previously. The dipole-dipole operator is again spin-dependent like the contact operator resulting in much cancellation between contributions from the two  $1s$  electrons. However, it differs in that it involves a spatial part which is tensorial in character with  $l=2$  dependence which results in differences in the nature of the excited states that are required in the diagrams. Further, the radial part of the operator is  $1/r^3$  as was the orbital operator. Thus any diagram calculated for the orbital interaction need only be multiplied by an angular factor to give the corresponding dipolar contribution.

Again the direct contribution which is the RHF result is given by the  $(0,0)$  diagram. This is diagram D1 in Fig. 12. The single  $(0,1)$  diagram is D2. This diagram represents anisotropic exchange polarization of the  $1s$  core by the  $2p$  electron. It is interesting to examine in more detail the distribution of the contributions to this type of diagram over the set of single-particle states. In Table II the various contributions to the contact  $(0,1)$  diagram and the dipole  $(0,1)$  diagram are compared. The contact contributions come from  $s$  bound and continuum states while only  $d$  states contribute to the dipolar diagram. This table makes clear the very special nature of the excited  $s$  states of this problem. Almost 70% of the value of the contact diagram comes from the  $2s$  orbital alone. In sharp contrast to this is the dipole case where over 99% comes from continuum states. This latter case is similar to the contact diagram in the earlier example<sup>3</sup> of Li ( $^2S$ ). The reason for the completely different behavior of the contact diagrams in the  $^2S$  and  $^2P$  cases is that for

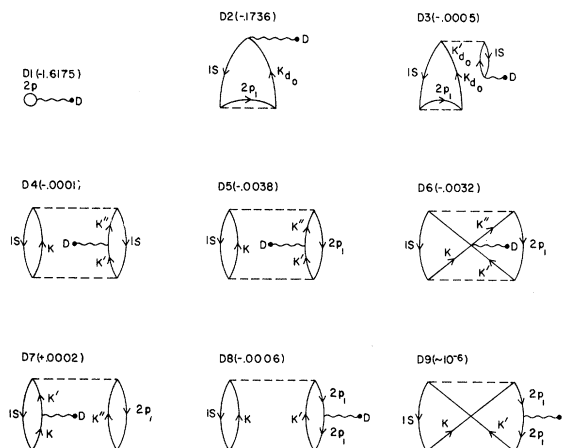


FIG. 12.  $(0,0)$ ,  $(0,1)$ , and  $(1,1)$  magnetic dipolar diagrams.

the latter the  $2s$  orbital is now available as an excited state. The  $2p$  hole state can have a strong interaction with the  $2s$  particle state by virtue of both the small energy difference and large overlap. For the  $^2S$  case, on the other hand, the nearest-bound particle state is  $3s$  which does not interact strongly with the  $2s$  hole state. Correspondingly for the  $(0,1)$  diagram D2 in Fig. 12, the nearest bound particle state is  $3d$  which explains the smaller effect of bound states in this case as well.

Another sharp contrast between the dipole-dipole and contact diagrams is seen in the hole-hole and hole-particle ladders of the  $(0,1)$  diagrams. In the contact case the total contribution from such ladders is quite negligible (0.02%) while ladders to the dipole-dipole diagram contribute over 40% of the total. This is not surprising since the  $d$  states were calculated in a potential appropriate for states of  $P$  symmetry. The ladder contribution corrects for the difference be-

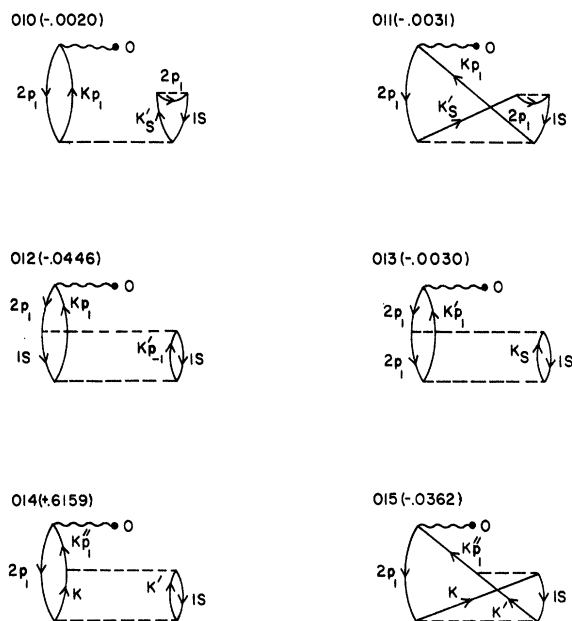


FIG. 11.  $(0,2)$  orbital interaction diagrams.

TABLE II. Contribution (in Mc/sec) to the contact and dipolar  $(0,1)$  diagrams from individual bound states and from the continuum. Values for the contact diagram represent contributions from  $s$  states while those for the dipolar diagram are from  $d$  states.

Source	Contact	Dipolar
$n=2$	-5.9227	•••
$n=3$	-0.2067	0.0004
$n=4$	-0.0608	0.0002
$n=5$	-0.0268	0.0001
$n=6$	-0.0142	0.0000
$n=7$	-0.0084	0.0000
$n=8$	-0.0054	0.0000
All bound	-6.2449	0.0006
Continuum	-2.3746	0.1730
Total	-8.6196	0.1736

tween the actual  $d$ -state potential and that assumed here.

The (1, 1) contribution consists of diagrams D3 through D9. The first of these is again an example of hybrid effects. All others represent various types of correlation. These diagrams are quite similar to the orbital case. Diagrams D4 and D7 are quite small since they enter only as residues. Diagrams D8 and D9 are of a type which has always been small. D5 and D6 are the largest diagrams for the same reason as given for O6 and O7 of Fig. 10.

The diagrams representing the (0, 2) contribution are given in Fig. 13. The first two of these represent ladder-like effects of employing a central potential approximation. The rest of the (0, 2) diagrams, D12 through D25, are further examples of hybrid and correlation effects.

#### D. Electric Quadrupole Interaction

As opposed to the magnetic interactions considered above, the field-gradient operator corresponds to an electrostatic polarization. The spatial part of the operator is identical with the dipole-dipole operator which leads to certain similarities in the diagrams of the two cases. However, the spin independence of the quadrupole operator as well as its electrostatic nature introduces additional diagrams not encountered previously. As indicated earlier we will consider the quadrupole-shielding factor  $\gamma$  explicitly, rather than the gradient  $q$  itself. Thus if the value of  $q$  is desired, it may be obtained from the diagrams simply by multiplying with  $q_0 = -0.0234a_B^{-3}$  obtained from Eq. (29).

In this case there are two (0, 1) diagrams as shown in Fig. 14 (Q1 and Q2). The first of these is again the result of anisotropic exchange polarization as seen in the dipole case. Diagram Q2, on the other hand, appears for the first time since it is associated with purely electrostatic quadrupole

polarization of the 1s core by the valence electron. Both of these effects were first identified by Sternheimer.<sup>19</sup> Of the (1, 1) diagrams, Q4 through Q10 are quite similar to those obtained for the magnetic dipolar interaction. Diagram Q3 is a hybrid effect of correlation with electrostatic polarization which occurs here for the first time.

In (0, 2) order the number of diagrams is larger than in any of the magnetic cases because of the addition of electrostatic effects and lack of cancellation due to spin. These diagrams are given in Fig. 15 and include various hybrid and correlation effects similar to diagrams contributing to the dipole interaction, Fig. 13. The dominant (0, 2) diagram, Q12, contributing to  $\gamma$  is of the new hybrid type, being a combination of electrostatic polarization and intrashell correlation effects.

#### IV. RESULTS AND DISCUSSION

The value of every diagram for each of the interactions is given in the previous section. These results are summarized in Table III. The contributions to each operator from (0, 0), (0, 1), (1, 1), and (0, 2) orders are shown in this table together with the totals. As seen here the results show marked decreases with increasing order in the perturbation. And in addition, as shown for the contact interaction in Fig. 9, diagrams of the next higher order are more than an order of magnitude smaller. Loosely speaking the (0, 0) and (0, 1) contributions are one-electron effects while (1, 1) and (0, 2) orders introduce many-body corrections. This relationship will be clarified in a comparison with specific other methods employed in calculations on this system.

We first turn our attention to one-electron perturbation theory approaches which have been used

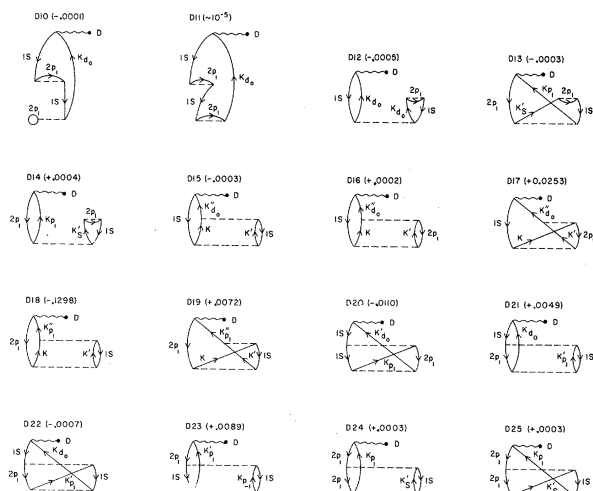


FIG. 13. (0, 2) diagrams for the magnetic dipole interaction.

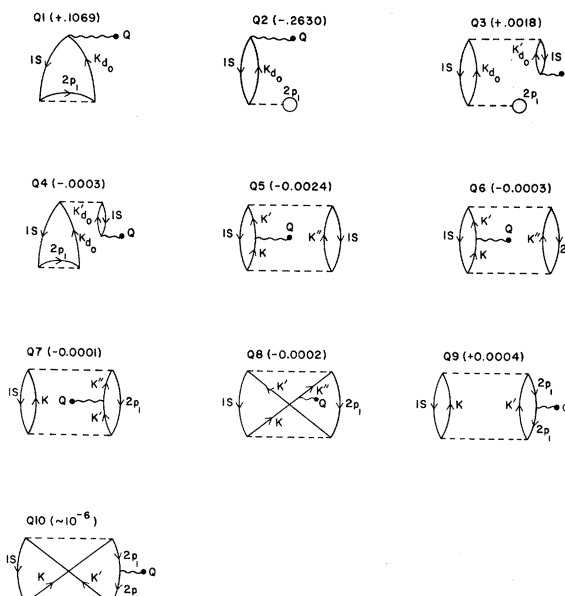


FIG. 14. Nuclear quadrupole shielding factor diagrams up to (1, 1) order.

to obtain exchange polarization corrections to magnetic hfs and the Sternheimer shielding factor. The results of these calculations should agree exactly with our (0, 1) diagrams for each interaction with the following qualifications. The (0, 1) diagrams must be considered as including all ladders arising as corrections to the particle states while, in the differential equation approaches, small differences are introduced by the use of a localized exchange potential. In view of these facts we find good agreement between results of the two approaches as seen from Table IV. In this table the method referred to as MP is a calculation of the interaction energy between the valence electron and the  $1s$  core perturbed by the nuclear magnetic or quadrupole moment. The EP method involves an application of these perturbations in the reverse order. These calculations of the magnetic interactions utilized the same zero-order Hartree-Fock wave function<sup>21</sup> as used in the present calculation. On the other hand, the shielding factor calculation used a wave function obtained from an empirical potential<sup>22</sup> and may be expected to indirectly include some correlation. However, the results of our calculation of  $\gamma$  (see Table III) show that correlation effects are not of great importance in this case. Thus we compare the strictly one-electron part of our calculation, the (0, 1) diagrams, with Sternheimer's one-electron procedure. These results are seen to differ by a factor of about 30%. Since the two procedures are very different, it is impossible to pinpoint the reason for this discrepancy. Two likely sources are the use of quite different starting wave functions and Sternheimer's use of a localized potential approximation. It is interesting to note that the MP calculation of  $a_{d\frac{3}{2}}$  of Rao *et al.*<sup>11</sup> is

TABLE III. Contributions from each order to the three types of magnetic hyperfine interaction and the nuclear quadrupole shielding constant for the  $J = \frac{3}{2}$  state.

Order	$a_C \frac{3}{2}$ (Mc/sec)	$a_O \frac{3}{2}$ (Mc/sec)	$a_{d\frac{3}{2}}$ (Mc/sec)	$\gamma$
(0, 0)	0	+8.0877	-1.6175	...
(0, 1)	-8.6196	0	-0.1736	-0.1561
(1, 1)	-0.4701	+0.0578	-0.0081	-0.0013
(0, 2)	-0.4786	+0.5270	-0.0951	-0.0126
Total	-9.5683	+8.6725	-1.8943	-0.1700

closely related to the exchange part of Sternheimer's result. The fact that there are similar discrepancies between these two one-electron results and our corresponding (0, 1) diagrams indicates that it is likely that the localized approximation, common to both, is responsible.

We consider the unrestricted Hartree-Fock (UHF) method separately from the other one-electron approaches since it includes consistency and some accidental correlation<sup>23</sup> effects. In order to compare our results with the UHF value for the contact term, it is more meaningful to combine the hybrid diagrams C2, C7, and C8 with our (0, 1) diagram. This gives a total of -10.57 Mc/sec which is in good agreement with Gooding's UHF result<sup>9</sup> of -10.7 Mc/sec. The difference between this value and our final contact result in Table III is a consequence of correlation effects not included in the UHF approach.

Before comparing our results with experimental measurements we will discuss the reliability of our calculation. Possible sources of error in this work are the truncation of sums over angular

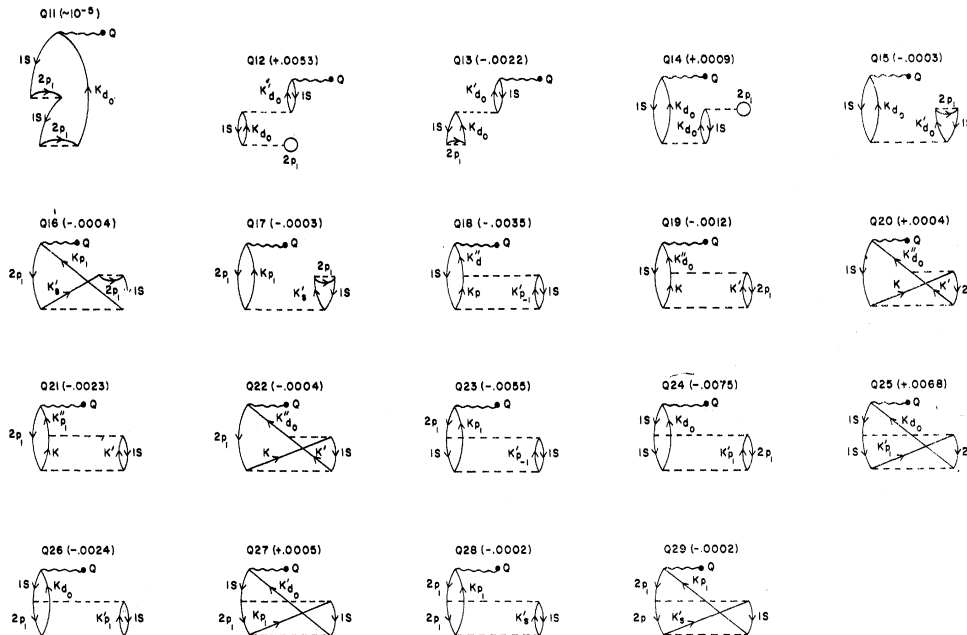


Fig. 15. (0, 2) diagrams for the quadrupole shielding factor.

TABLE IV. Comparison of (0, 1) diagrams with earlier one-electron core-polarization calculations.

Method	$a_{c\frac{3}{2}}$ (Mc/sec)	$a_{d\frac{3}{2}}$ (Mc/sec)	Sternheimer shielding factor		
			Direct	Exchange	Total
MP	-8.9 <sup>a</sup>	-0.1113 <sup>c</sup>	-0.1819 <sup>d</sup>	+0.0663 <sup>d</sup>	-0.1156 <sup>d</sup>
EP	-8.5 <sup>b</sup>	...	...	...	...
(0, 1) diagram	-8.6196	-0.1736	-0.2630	+0.1069	-0.1561

<sup>a</sup>See Ref. 10.<sup>b</sup>M. H. Cohen, D. A. Goodings, and V. Heine, Proc. Phys. Soc. (London) 73, 811 (1959).<sup>c</sup>See Ref. 11.<sup>d</sup>See Ref. 12.

momentum states at  $l=3$ , truncation of the wave function after second order in  $\Delta\mathcal{H}$ , and numerical accuracy of the computations. The effect of considering only up to  $f$  angular momentum states was discussed briefly in connection with Table I. As seen in that typical example there is a definite decrease in the size of the contributions in going from  $s$  to  $f$  states. Furthermore there are few diagrams in which  $f$ -state contributions are allowed at all and their total effect on the coupling constant is quite small. Thus, while it is clear that higher  $l$  states will contribute in a few cases, we are confident that the total for all remaining  $l$  values will be very small. Our conservative estimate is that the error resulting from this source is less than 0.5%. The second subject to be considered in this discussion is convergence in orders of perturbation theory. The value of Brueckner-Goldstone perturbation theory as a computational tool for atomic problems certainly rests in large measure on whether the wave function to second order has converged sufficiently to give accurate results. For larger atomic systems it would be prohibitively difficult to calculate the third-order wave function by techniques heretofore employed. However, we feel the present calculation gives strong evidence that at least for hyperfine effects, the second-order wave function is extremely good. In Table III we have given the sums of all contributing diagrams in each order of the perturbation. The higher-order values there are significantly smaller than those of lower order. Even more revealing is the fact that (0, 3) and (1, 2) diagrams of the types which predominate in lower orders have dropped off by at least another order of magnitude. And, in addition, because of our choice of potential and the nature of the particular operators being considered, the majority of diagrams of high orders can contribute only as residues. Thus we feel that inclusion of all diagrams from higher orders in the perturbation,  $\Delta\mathcal{H}$ , would not change the calculated result by more than 1%. The third of the possible sources of error mentioned above is the actual accuracy of the numerical approximations. This consists mainly of the error inherent in the numerical technique for integrating the one-electron equation, Eq. (4), and in the integration formulas utilized in

both coordinate and momentum space for evaluating the diagrams. This total computational error is estimated to be well under 0.1%. As the result of the foregoing considerations, we feel that a conservative estimate of the error limits of our calculated results for each of the interactions is about 1.5%. Thus, for example, the approximate error range in the contact parameter,  $a_{cJ}$ , is  $\pm 0.15$  Mc/sec.

As indicated previously the only experimental value available for this system is  $a_{1/2}$ . In order to compare with this result we must utilize Eqs. (36) through (38) to obtain  $a_{i\frac{1}{2}}$  from  $a_{i\frac{3}{2}}$ . Our values thus obtained are

$$a_{c\frac{1}{2}} = 9.5683 \text{ Mc/sec}, \quad (43)$$

$$a_{o\frac{1}{2}} = 17.3450 \text{ Mc/sec}, \quad (44)$$

$$a_{d\frac{1}{2}} = 18.9430 \text{ Mc/sec}, \quad (45)$$

giving a total of

$$a_{\frac{1}{2}} = 45.8563 \text{ Mc/sec}. \quad (46)$$

The experimental measurement of  $a_{\frac{1}{2}}$  by Ritter<sup>14</sup> yielded the result

$$(a_{\frac{1}{2}})_{\text{expt}} = 46.17 \pm 0.35 \text{ Mc/sec}. \quad (47)$$

Thus our value is within the experimental error bars and, in fact, differs from Ritter's value by less than 0.7%.

Ardill and Stewart<sup>13</sup> have published a configuration interaction calculation of the hfs of Li (<sup>2</sup>P) based on a 45-term wave function of Weiss.<sup>24</sup> However, the specific form of the configurations included is such that the excitation required to provide the anisotropic exchange polarization contribution is not present. Thus we would not expect this effect to be adequately taken into account in their calculation. Their value for  $a_{1/2}$  is 45.70 Mc/sec, in quite good agreement with ours. However, this agreement is questionable since their contact result, 12.85 Mc/sec, differs markedly

from ours and all other calculations of this parameter. They have quoted only the total of the orbital and dipolar interactions combined, giving 32.85 Mc/sec, to be compared with our result of 36.2880 Mc/sec. This again demonstrates the advantage of the BG technique in that no arbitrary choice of configurations has to be made and thus no important contributions missed.

As shown in Sec. II our single calculation yields both the results for  $J = \frac{1}{2}$  and  $J = \frac{3}{2}$ . Thus our value for  $a_{3/2}$  is just as accurate as that given for  $a_{1/2}$ . This value is

$$a_{3/2} = -2.7906 \text{ Mc/sec.} \quad (48)$$

Since no direct measurement of this quantity is available, we would hope to encourage experimental verification of this theoretical prediction. At the present time the closest to an experimental result for  $a_{3/2}$  that has appeared is a calculation from level-crossing data by Brog, Eck, and Wieder.<sup>15</sup> This derivation was based on the one-electron theory and did not consider anisotropic exchange polarization. In fact their value for  $a_{3/2}$  of  $-3.40 \pm 0.23$  Mc/sec is based on the assumption that the one-electron relation  $(a_{O\frac{1}{2}} + a_{d\frac{1}{2}}) = 5(a_{O\frac{3}{2}} + a_{d\frac{3}{2}})$  will hold in general. As seen from our results the many-electron version of this ratio is actually

$$(a_{O\frac{1}{2}} + a_{d\frac{1}{2}}) = 5.35(a_{O\frac{3}{2}} + a_{d\frac{3}{2}}) \quad (49)$$

which is a significant change from the one-electron equation. A similar comment applies to their level-crossing relationship. It should be noted here that, by utilizing the accurate values obtained in this calculation for the matrix elements of each of the interactions over various  $M_L M_S$  states, a detailed and accurate analysis of the level-crossing experiment is possible. This could be utilized either to make theoretical predictions of the level-crossing field values or alternatively to obtain values of the hyperfine constants appropriate to the  $J = \frac{3}{2}$  level from the experimental level-crossing fields.<sup>25</sup>

The quadrupole moment  $Q$  may be obtained from the interaction energy

$$W = -e^2 a_B^{-3} q Q \text{ (cgs).} \quad (50)$$

The negative sign on the right of Eq. (50) occurs because the field gradient  $q$  of Eq. (27) arising from electrons must be multiplied by  $-ea_B^{-3}$  to obtain  $W$  in cgs units. Brog *et al.* obtained  $-0.18 \pm 0.12$  Mc/sec for  $W$ . Thus using Eq. (28) for  $q$  in terms of the shielding factor  $\gamma$  our result for the quadrupole moment of Li<sup>7</sup> is

$$Q = (-3.9 \pm 2.6) \times 10^{-26} \text{ cm}^2. \quad (51)$$

This result is quite a bit larger in magnitude than the value given by Brog *et al.* of  $(-3 \pm 2) \times 10^{-26}$  cm<sup>2</sup>. The difference can easily be accounted for in that their calculation is entirely one electron in nature and also they did not employ a shielding factor for  $q$ . Kahalas and Nesbet<sup>26</sup> have published a value of  $Q = -4.4 \times 10^{-26}$  cm<sup>2</sup> using a measurement of the quadrupole coupling constant of LiH by Wharton, Gold, and Klemperer.<sup>27</sup> Our result agrees well with theirs both in sign and magnitude. It is hoped that a technique may be devised whereby a more reliable measurement of  $W$  will be possible, thus enabling a more accurate determination of  $Q$ .

We have demonstrated for the first time in this paper the use of the BG technique for obtaining all the hyperfine properties of a nonspherical system. The results have been shown to be quite accurate and in excellent agreement with experiment. It is to be hoped that this calculation will encourage further experimental analysis of lithium in the  $^2P$  state. From a theoretical point of view, our success in this system, combined with similar favorable experience in spherical systems, suggest that it would be fruitful to use this procedure in larger atomic and molecular systems. Not only would this enable us to bridge the gap between one-electron theory and experiment, but also in the process provide an improved understanding of the role of many-electron effects.

#### ACKNOWLEDGMENT

The authors are indebted to R. K. Nesbet and P. G. H. Sandars for several discussions which greatly clarified a number of points of importance to this work. We are also grateful to N. C. Dutta, Miss C. Matsubara, and Dr. T. Ishihara for considerable help throughout much of this investigation.

\*Supported in part by the National Science Foundation.

<sup>1</sup>J. Goldstone, Proc. Roy. Soc. (London), Ser. A **239**, 267 (1957).

<sup>2</sup>H. P. Kelly, *Perturbation Theory and its Application in Quantum Mechanics*, edited by C. H. Wilcox (John Wiley & Sons, Inc., New York, 1966), p. 215; see also Phys. Rev. **131**, 684 (1963); **136**, B896 (1964); **144**, 39 (1966).

<sup>3</sup>E. S. Chang, R. T. Pu, and T. P. Das, Phys. Rev. **174**, 1 (1968); see also E. S. Chang, Ph. D. thesis, University of California, Riverside, 1967 (unpublished).

<sup>4</sup>C. Matsubara, N. C. Dutta, R. T. Pu, and T. P. Das, Bull. Am. Phys. Soc. **13**, 373 (1968).

<sup>5</sup>N. C. Dutta, C. Matsubara, R. T. Pu, and T. P. Das, Phys. Rev. **177**, 33 (1969).

<sup>6</sup>N. C. Dutta, C. Matsubara, R. T. Pu, and T. P.

Das, Phys. Rev. Letters 21, 1139 (1968).

<sup>7</sup>Portions of this work were reported briefly at the Pasadena meeting of the American Physical Society, December, 1967, Bull. Am. Phys. Soc. 12, 1116 (1967).

<sup>8</sup>H. P. Kelly in a paper, Phys. Rev. 173, 142 (1968), (kindly sent to us prior to publication) on oxygen, which is also nonspherical, has analyzed by the BG technique the contact hyperfine interaction, which however is not sensitive to the nonsphericity.

<sup>9</sup>D. A. Goodings, Phys. Rev. 123, 1706 (1961).

<sup>10</sup>G. D. Gaspari, Wei-Mei Shyu, and T. P. Das, Phys. Rev. 134, A852 (1964).

<sup>11</sup>B. K. Rao, Dennis Ikenberry, S. D. Mahanti, and T. P. Das, to be published.

<sup>12</sup>R. M. Sternheimer, Phys. Rev. 164, 10 (1967).

<sup>13</sup>R. W. B. Ardill and A. L. Stewart, Proc. Phys. Soc. (London) 92, 296 (1967).

<sup>14</sup>G. J. Ritter, Can. J. Phys. 43, 770 (1965).

<sup>15</sup>K. C. Brog, T. G. Eck, and H. Wieder, Phys. Rev. 153, 91 (1967).

<sup>16</sup>The function  $\Psi$  here has the same significance as  $\Psi_0$  of Ref. 3, the suffix zero having been dropped here to distinguish the excited state from the ground state. Correspondingly,  $\Psi_0$  in Eq. (5) has the same meaning

as  $\Phi_0$  in Ref. (3).

<sup>17</sup>M. E. Rose, *Relativistic Electron Theory* (John Wiley & Sons, Inc., New York, 1961).

<sup>18</sup>M. Tinkham, *Group Theory and Quantum Mechanics* (McGraw-Hill Book Co., Inc., New York, 1964).

<sup>19</sup>R. M. Sternheimer and H. M. Foley, Phys. Rev. 102, 731 (1956); T. P. Das and R. Bersohn, Phys. Rev. 102, 733 (1956); see also R. M. Sternheimer, Phys. Rev. 80, 102 (1950); 84 244 (1951).

<sup>20</sup>J. S. M. Harvey, Proc. Roy. Soc. (London), Ser. A 285, 581 (1965).

<sup>21</sup>D. A. Goodings, Ph. D. thesis, Cambridge University, 1960 (unpublished).

<sup>22</sup>F. Seitz, Phys. Rev. 47, 400 (1935); W. Kohn and N. Rostoker, Phys. Rev. 94, 1111 (1954).

<sup>23</sup>V. Heine, Czech. J. Phys. 13, B619 (1963).

<sup>24</sup>A. W. Weiss, Astrophys. J. 138, 1262 (1963).

<sup>25</sup>This subject requires a somewhat specialized analysis and would be out of place here. The authors intend to present this in a later publication.

<sup>26</sup>S. L. Kahalas and R. K. Nesbet, J. Chem. Phys. 39, 529 (1963).

<sup>27</sup>L. Wharton, L. P. Gold, and W. Klemperer, J. Chem. Phys. 37, 2149 (1962).

## Mean Lives of Some Doubly Excited Levels in Lithium I\*

William S. Bickel, † Ingmar Bergström, Rudolf Buchta, Lennart Lundin, and Indrek Martinson

*Research Institute for Physics, Stockholm 50, Sweden*

(Received 10 October 1968; revised manuscript received 18 November 1968)

Three doubly excited levels in Li I produced upon passage of 56-keV <sup>7</sup>Li ions through a thin carbon foil have been identified. Their mean lives were measured using the beam-foil technique with the results given below:

$$\begin{aligned}\tau(1s2p^2\ ^4P) &= (6.4 \pm 0.3) \times 10^{-9} \text{ sec}, \\ \tau(1s2s3s\ ^4S) &= (9.7 \pm 0.7) \times 10^{-9} \text{ sec}, \\ \tau(1s2s3d\ ^4D) &= (4.5 \pm 0.4) \times 10^{-9} \text{ sec}.\end{aligned}$$

In the optical spectrum of lithium certain spectral lines appear which cannot be assigned to the normal term schemes of Li I or Li II. It has been suggested by several authors<sup>1-4</sup> that these lines originate from radiative transitions between doubly excited quartet states in Li I, lying between the first and second ionization potential.

Due to selection rules these levels cannot auto-ionize through Coulomb interaction. Auto-ionization, because of magnetic interaction, is much

less likely and this process is too slow to compete with radiative decay to the lowest doubly excited level.

Four lines in the visible region classified as transitions between doubly excited levels are

$$\begin{array}{ll}1s2s3d\ ^4D \rightarrow 1s2s2p\ ^4P & \lambda 2337 \text{ \AA}, \\ 1s2s3s\ ^4S \rightarrow 1s2s2p\ ^4P & \lambda 2934 \text{ \AA}, \\ 1s2p^2\ ^4P \rightarrow 1s2s2p\ ^4P & \lambda 3714 \text{ \AA}, \\ 1s2p3p\ ^4P \rightarrow 1s2s3p\ ^4P & \lambda 4607 \text{ \AA}.\end{array}$$